Active damping control unit using a small scale proof mass electrodynamic actuator

Cristóbal González Díaz,[a] Christoph Paulitsch,[b] and Paolo Gardonio[c]
Institute of Sound and Vibration Research, University of Southampton, Southampton SO17 1BJ, United Kingdom

(Received 9 July 2007; revised 30 April 2008; accepted 23 May 2008)

This paper presents a study on the design and use of a small scale proof mass electrodynamic actuator, with a low mounting resonance frequency, for velocity feedback control on a thin rectangular panel. A stability-performance formula is derived, which can be effectively used to assess the down scaling effects on the stability and control performance of the feedback loop. The design and tests of a velocity feedback loop with a prototype small scale proof mass actuator are also presented. When a feedback control having a gain margin of about 6 dB is implemented, so that there is little control spillover effect around the fundamental resonance of the actuator, reductions of vibration between 5 dB and 10 dB in the frequency band between 80 Hz and 250 Hz have been measured at the control position. © *2008 Acoustical Society of America.* [DOI: 10.1121/1.2945167]

PACS number(s): 43.40.Vn, 43.50.Ki, 43.40.At [KAC] Pages: 886–897

I. INTRODUCTION

This paper presents a study on the design and practical implementation of a velocity feedback control loop on a thin rectangular panel with a small scale proof mass electrodynamic actuator. Particular emphasis is given to the scaling effects of reducing the actuator size on stability and control performance when direct velocity feedback is implemented. The aim of the scaling study is to provide general guidelines for the design of the prototype small scale proof mass actuator.

Sound radiation and transmission by thin, lightly damped, partitions are relevant problems both in land and air transportation vehicles. For instance, in order to improve the fuel consumption efficiency, the new designs of aircraft fuselage and automobile bodywork involve stiff and lightweight panels, which therefore efficiently radiate noise generated by external acoustic sources (i.e., jet noise or reciprocating engine noise), by aerodynamic sources (i.e., turbulent boundary layer pressure fields on aircraft skins or on car bodyworks), and by structure borne paths (i.e., engine induced vibrations or road induced vibrations).[1–3] Passive treatments, such as stiffening, mass, or damping treatments, can be used to reduce this problem[4,5] although, in order to be effective at low audio frequencies, they tend to be bulky and introduce extra weight that contrasts with the fuel consumption requirement. Recent research work has shown that decentralized active vibration control with point force actuators provides an efficient solution to the low frequency sound transmission problem.[6]

At low frequency, the sound radiation by a lightly damped panel is characterized by well separated resonances of the low order modes of the panel.[7,8] Thus, steady state broad band sound radiation can be effectively reduced by tackling the low frequency resonances of the panel itself[6,8] without the need to involve control arrangements with complicated sensor and actuator pairs that operate on the sound radiation modes of the structure.[9–11] In general, the resonant response of structures is governed by damping, which can be effectively controlled by active systems that produce damping actions.[7] This can be achieved with simple direct velocity feedback control systems.[12]

If ideal point force actuators and velocity sensors are used, then collocated velocity feedback is bound to be unconditionally stable.[13,14] In practice, force actuators are constructed with an electrodynamic actuator that reacts off a proof mass. This type of actuator produces a constant force above the fundamental resonance frequency of the resiliently mounted mass.[12] Thus, they must be designed with a relatively low fundamental resonance frequency, which must be well below the first resonance frequency of the structure to be controlled. Also, Elliott *et al.*[15] have shown that in order to guarantee large control gains, this actuator fundamental resonance must be well damped.

Theoretical work has shown that, in order to effectively produce damping on panels with point actuators, several velocity feedback loops should be implemented.[6] The control bandwidth tends to rise with the number of control units.[10] Thus, it is necessary to design small scale control systems which withstand the necessary stability requirements for the implementation of direct velocity feedback loops and produce the largest possible damping effect.

This paper introduces the stability and performance study of a small scale prototype electrodynamic proof mass actuator for the implementation of a direct velocity feedback loop on a thin panel structure. In Sec. II, a mobility/impedance formulation is presented which provides a simple "stability-performance" formula that can be used to assess simultaneously the stability and control performance of the feedback control loop with the proof mass actuator. In Sec.

[a]Electronic mail: cgd@isvr.soton.ac.uk
[b]Electronic mail: cpaulits@gmx.de
[c]Electronic mail: pg@isvr.soton.ac.uk

TABLE I. Geometry and physical parameters for the clamped aluminium panel.

Parameter	Value
Dimensions	$l_x \times l_y = 414 \times 314$ mm^2
Thickness	$h = 1$ mm
Mass density	$\rho = 2720$ kg/m^3
Young's modulus	$E = 7.1 \times 10^{10}$ N/m^2
Poisson ratio	$\nu = 0.33$
Damping loss factor	$\eta = 0.02$
Coordinates of primary force excitation	$x_p, y_p = 341,246$ mm
Coordinates of control point	$x_c, y_c = 109,75$ mm
Mass of the force transducer for the primary excitation	$M_s = 30$ g

TABLE II. Geometry and physical parameters for the actuator.

Parameter	Value
Proof mass diameter	24 mm
Proof mass height	12 mm
Magnet diameter	18 mm
Magnet height	9.3 mm
Base disk diameter	38 mm
Base disk thickness	1 mm
Housing and base disk mass	$M_b = 8$ g
Proof mass	$M_a = 22$ g
Suspension system stiffness	$K_a = 347.4$ N/m
Suspension system damping	$C_a = 3.3$ N/m s^{-1}
Fundamental natural frequency	$f_a = 20$ Hz
Vioce coil coefficient	$\psi = 2.6$ N/A

III, the principal downscaling and design issues of the proof mass actuator are discussed in view of the stability requirements and control performance properties of the feedback loop. In particular, the scaling laws are derived for (a) the fundamental natural frequency ω_a, (b) the static displacement δ_a, (c) the current in the coil windings i_a, (d) the generation of electrodynamic force f_a and transmitted force f_c, (e) the stroke of the suspended mass Δw, (f) the maximum gain that guarantees stability $g_{\max}$, and (f) the "control performance ratio" R_k. The design and experimental tests of a prototype velocity feedback control unit with a small scale proof mass actuator are then presented in Sec. IV. In particular, the stability and control performance are discussed with reference to the Nyquist criterion applied to the locus of the open loop sensor-actuator Frequency Response Function (FRF).

II. DIRECT VELOCITY FEEDBACK CONTROL USING A PROOF MASS ACTUATOR

Before entering into the details of the downscaling study, the principal characteristics of force actuation with a proof mass electrodynamic actuator mounted on a rectangular panel are considered. This analysis has been carried out with reference to the panel and prototype actuator considered in Sec. IV whose geometrical and physical properties are summarized in Tables I and II. The stability and control performance of a negative velocity feedback loop using this type of actuator are examined with a simple stability-performance formula which derives the reduction of vibration at the control position for the maximum gain of the feedback control loop that guarantees stability. The scaling laws of the principal mechanical and electrodynamic components are then derived and used to assess the downscaling effect on the stability and control performance of the control unit.

A. Actuation mechanism

As schematically shown in Fig. 1(a), the control system considered in this study uses a coil-magnet electrodynamic linear motor. The coil is fixed to the base of the actuator and the magnet is suspended on springs so that it provides the inertial reaction necessary to generate a point force f_c on the structure where the actuator is fixed.[12]

Figure 1(b) shows the equivalent electromechanical schematic that has been used to model the response of this actuator when it is fixed on a clamped rectangular aluminum panel. The model takes into account the inertial effect of the proof mass and stiffness-damping effects of the suspension system. In order to keep the formulation simple, the inertial effect of the base and coil masses is instead neglected. Assuming time harmonic vibratory motion of the form $\exp(j\omega t)$, where ω is the circular frequency and $j = \sqrt{-1}$, the fully coupled response of the plate and actuator system has been derived by considering the following mobility and impedance equations:

$$\dot{w}_c = Y_{cc} f_c + Y_{cp} f_p, \tag{1}$$

$$\dot{w}_m = Y_a f_m, \tag{2}$$

$$f_c = -Z_a \dot{w}_c + Z_a \dot{w}_m - f_a \tag{3}$$

and

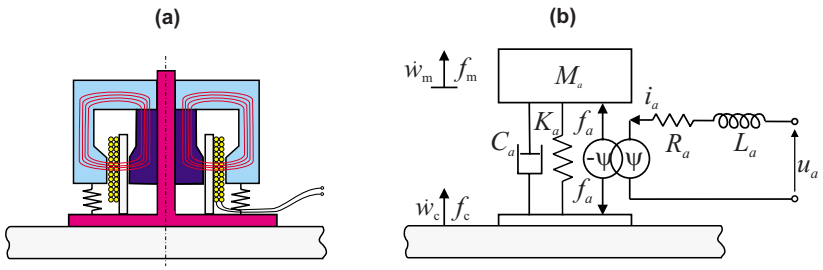

FIG. 1. (Color online) Proof mass electrodynamic force actuator: (a) sketch; (b) electromechanical schematic. As shown in (a), the proof mass is formed by a magnetic core cylinder and an outer ferromagnetic ring.

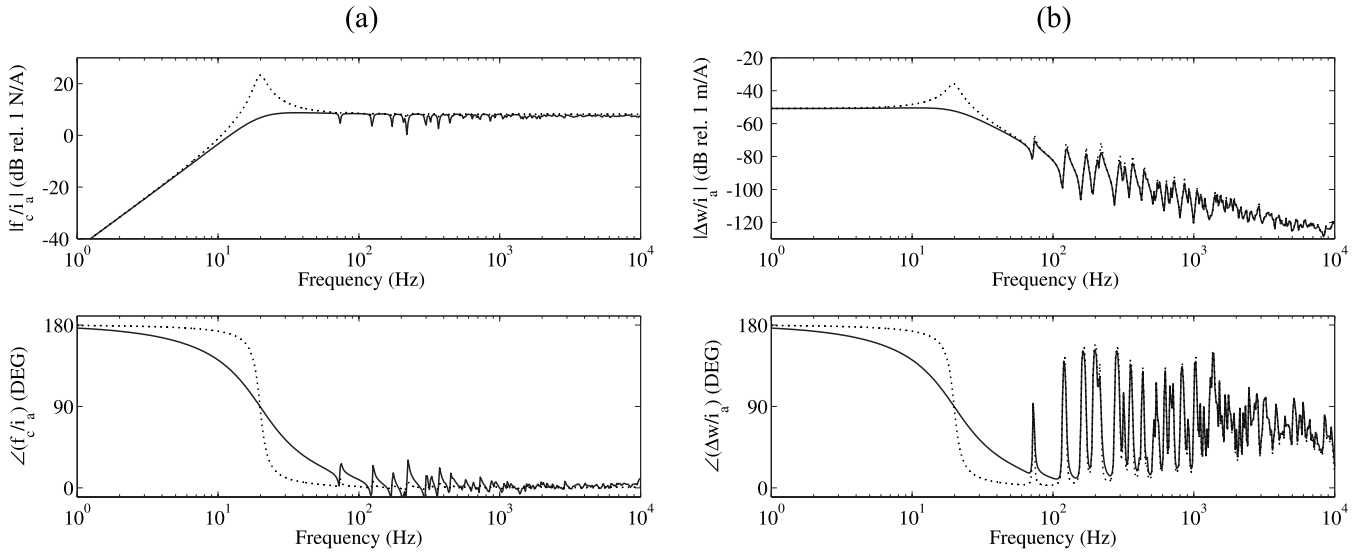

FIG. 2. (a) Simulated force transmitted to the plate per unit driving current. (b) Simulated stroke per unit driving current. Thick lines heavily damped actuator (C_a=3.3 N/m s^{-1}), dotted lines lightly damped actuator (C_a=0.5 N/m s^{-1}).

$$f_m = Z_a \dot{w}_c - Z_a \dot{w}_m + f_a, \tag{4}$$

where $\dot{w}_c(\omega)$, $\dot{w}_m(\omega)$, $f_c(\omega)$, and $f_m(\omega)$, are, respectively, the complex velocities and forces at the base and proof mass components of the actuator and $f_p(\omega)$ is the complex primary force excitation acting on the plate. $Y_{cc}(\omega)$ and $Y_{cp}(\omega)$ are the plate mobility functions, respectively, at the point where the actuator is attached and between the point where the actuator is attached and the location of the primary force. The two mobility functions have been derived in terms of the following modal summations:[16]

$$Y_{cc} = j\omega \sum_{n=1}^{N} \frac{[\phi_n(x_c,y_c)]^2}{M_p[\omega_n^2(1+j\eta)-\omega^2]}, \tag{5}$$

$$Y_{cp} = j\omega \sum_{n=1}^{N} \frac{\phi_n(x_c,y_c)\varphi_n(x_p,y_p)}{M_p[\omega_n^2(1+j\eta)-\omega^2]}, \tag{6}$$

where M_p is the mass of the plate, η is the loss factor, and ω_n and $\phi_n(x,y)$ are, respectively, the nth natural frequency and nth natural mode of the plate at position (x,y), which have been taken from Ref. 16 for a clamped plate. Finally, $Z_a(\omega)$ and $Y_a(\omega)$ are the impedance and mobility functions for the spring-dashpot and proof mass components of the actuator:[16]

$$Z_a = \frac{K_a}{j\omega} + C_a, \tag{7a}$$

$$Y_a = \frac{1}{j\omega M_a}, \tag{7b}$$

where K_a, C_a, and M_a are, respectively, the stiffness, viscous damping coefficient, and mass of the three components of the actuator.

Assuming the actuator is driven by current, i_a, so that

$$f_a = -\psi i_a, \tag{8}$$

where ψ is the voice coil factor of the actuator;[12] using Eqs. (1)–(4), the force transmitted to the base f_c and the stroke of the suspended mass with reference to the base of the actuator $\Delta w = w_m - w_c$ are given by

$$f_c = \frac{\psi}{1 + Z_a(Y_a + Y_{cc})} i_a, \tag{9}$$

$$\Delta w = -\frac{1}{j\omega} \frac{(Y_a + Y_{cc})\psi}{1 + Z_a(Y_a + Y_{cc})} i_a. \tag{10}$$

The plot in Fig. 2(a) shows the spectrum of the transmitted force f_c per unit driving current i_a. Considering first the case where the actuator is lightly damped (dotted line), at frequencies below the fundamental resonance frequency of the actuator, the transmitted force f_c is out of phase with the driving current signal and monotonically rises from zero up to a maximum value at the fundamental resonance of the actuator at about 20 Hz. At higher frequencies, the transmitted force f_c is in phase with the driving current signal and its amplitude levels down to a constant value which is approximately equal to the reactive forces f_a generated by the coil-magnet linear motor.[12] The narrow band troughs of the amplitude are due to the low impedance effect produced by the plate at resonance frequencies. When the actuator is heavily damped (thick line), the actuator resonance peak is smoothed down and can hardly be seen. Also, the transition from out of phase to in phase force actuation is stretched out over a wider frequency band. In conclusion, if negative velocity feedback is implemented, the desired damping action is produced only above the fundamental resonance of the actuator. In contrast, below this frequency, negative damping is generated, which tends to destabilize the control loop. This observation already offers a key indication about the fundamental issue of this type of actuator, that is, the actuator should be designed with the smallest possible fundamental resonance frequency in order to ensure a constant force excitation in a wider range of low audio frequencies where the active damping effect is mostly desired.

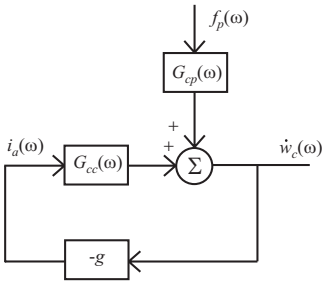

FIG. 3. Block diagram of the velocity feedback control loop using a current driven electrodynamic proof mass actuator.

The plot in Fig. 2(b) shows the spectrum of the stroke Δw per unit driving current i_a. Considering first the case where the actuator is lightly damped (dotted line), at frequencies below the fundamental resonance frequency of the actuator, the stroke is out of phase with the driving current signal. According to Eq. (10), for $\omega=0$, the stroke per unit current is given by $\Delta w=-(\psi/K_a)i_a$. The amplitude of the stroke tends to remain constant up to frequencies close to the fundamental resonance of the actuator at about 20 Hz where it becomes maximum. At higher frequencies, the stroke is in phase with the driving current signal and its amplitude rolls off monotonically with frequency. Between 100 Hz and 1 kHz, the amplitude of the spectrum of the stroke is characterized by a sequence of resonance peaks due to the low order natural modes of the panel. As the frequency rises, the modal overlap in the plate increases so that the amplitude spectrum of the stroke becomes smoother above 1 kHz. As found for the control force f_c, when the actuator is heavily damped, the actuator resonance peak is smoothed down and the phase transition from +180° to 0° is stretched out over a wider frequency band. In conclusion, the maximum stroke produced by the actuator is at the fundamental resonance of the actuator at about 20 Hz.

Substituting Eq. (10) into Eq. (9), the transmitted force f_c can be expressed in terms of the stroke of the proof mass

$$f_c = -\frac{j\omega}{(Y_a + Y_{cc})}\Delta w. \tag{11}$$

This expression highlights that the transmitted force f_c depends on the stroke of the proof mass via the impedance $Z_{pa}=1/(Y_a+Y_{cc})$ offered by the proof mass and the plate at the control point. Thus, for a given maximum current i_a that can be fed to the actuator without damaging the coil and for a maximum stroke Δw that the suspended mass can withstand, without hitting the end stops of the actuator, the force transmitted f_c to the base of the actuator can be enhanced by increasing the proof mass so that the plate-actuator impedance Z_{pa} also rises.

B. Stability of a direct velocity feedback loop

Assuming the error sensor for the feedback loop is an ideal velocity sensor located at the base of the actuator, in which case it measures exactly $\dot{w}_c$, the response of the panel measured by the error sensor can be modeled in terms of the classic disturbance rejection feedback block diagram shown in Fig. 3, where $G_{cc}(\omega)$ and $G_{cp}(\omega)$ are the fully coupled FRFs between the error sensor velocity $\dot{w}_c$ and either the control current i_a or primary force excitation f_p, which can be derived from Eqs. (1)–(4):

$$G_{cc}(\omega) = \frac{\dot{w}_c}{i_c} = \frac{Y_{cc}\psi}{1 + Z_a(Y_a + Y_{cc})}, \tag{12}$$

$$G_{cp}(\omega) = \frac{\dot{w}_c}{f_p} = \frac{(1 + Z_a Y_a)Y_{cp}}{1 + Z_a(Y_a + Y_{cc})}. \tag{13}$$

Figure 4 shows the Bode and Nyquist plots of the open loop sensor-actuator FRF $gG_{cc}(\omega)$ assuming $g=1$. The Bode plot shows that the modulus of $G_{cc}(\omega)$ is characterized by a heavily damped resonance at about 20 Hz, which is due to the actuator fundamental natural mode, and then a sequence of resonance peaks, which are due to the low order natural modes of the plate. The phase of $G_{cc}(\omega)$ starts from +270° at low frequency, drops to +90° beyond the resonance of the actuator, and then it alternates between +90° and −90° for the resonances of the plate. As a result, the Nyquist plot shows that the loci of $G_{cc}(\omega)$ is characterized by one circle in the left hand side quadrants, which is due to the resonance of the actuator, and many circles in the right hand side quadrants, which are due to the resonances of the plate. Therefore, using the Nyquist stability criterion,[17] the control system is found to be only conditionally stable since, for relatively high control gains, the circle on the left hand side due to the fundamental resonance of the actuator can enclose the Nyquist instability point $-1+j0$. Also, for control gains that ensure stability, the circle in the left hand side quadrants indicates that control spillover is bound to occur around the fundamental resonance frequency of the actuator.

In summary, the stability and control performance of a velocity feedback control loop with a proof mass actuator are heavily affected by the presence of the fundamental resonance of the actuator. In order to guarantee a stable feedback control loop with high control gains, it is necessary to reduce the amplitude of the actuator resonance so that the left hand side circle in the Nyquist plot would be small. Nevertheless, when large control gains are implemented, undesired control spillover effect takes place.

In order to reduce the amplitude of the first resonance peak of $G_{cc}(\omega)$, the fundamental natural frequency of the actuator should be kept as low as possible. This can be achieved by designing the proof mass suspension system with very soft springs. However, with a too soft suspension system, the static displacement of the proof mass becomes too big so that practical problems, such as nonlinearity due to the proof mass striking the end stops of the actuator, may disrupt the stability of the feedback control loop.[18] The amplitude of the fundamental resonance of the proof mass actuator can also be lowered by increasing the damping effect in the actuator. However, this approach is also affected by practical problems, which again may involve nonlinearity.

C. Control performance

As discussed above, the velocity feedback control system considered in this paper is devised to produce active damping, which efficiently reduces the response around the

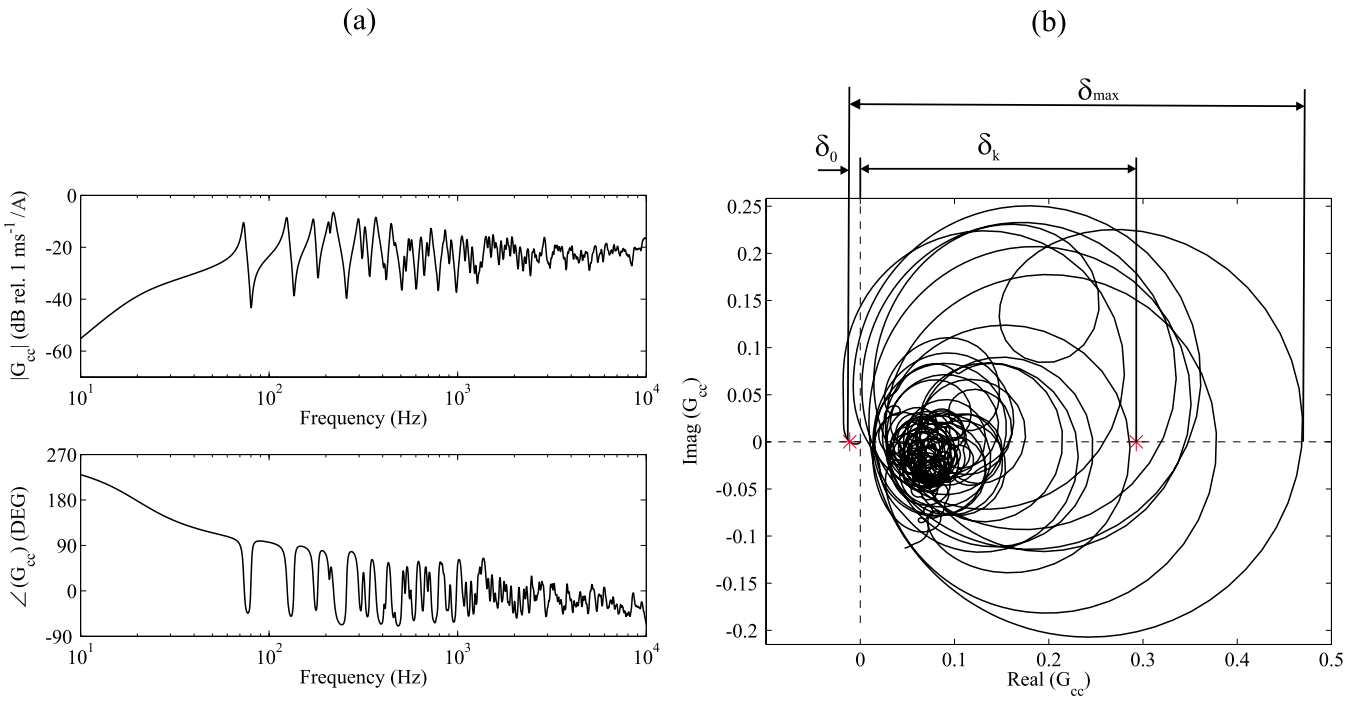

FIG. 4. (Color online) Bode (a) and Nyquist (b) plots of the simulated open loop sensor-actuator FRF $gG_{cc}(\omega)$, assuming $g=1$ when a proportional feedback loop is used for current control.

resonance frequencies of low order modes of the panel. Thus, the effectiveness of the control system can be evaluated by looking to the reduction of vibration that can be achieved at each resonance frequency of the panel rather than over the whole frequency band. The active damping effect produced by each control unit can be assessed by considering the reduction of vibration at the control position, although it should be noted that this does not directly correspond to a mean reduction of vibration over the panel surface. In fact, as discussed in Ref. 19 for too high control gains, the control units produce a pinning effect at the control position which simply rearranges the spatial vibration of the panel and does not inject damping to the structure.

According to the block diagram in Fig. 3, the responses at the control position per unit primary excitation with and without feedback control are, respectively, given by

$$\frac{\dot{w}_{c/c}}{f_p} = \frac{G_{cp}}{1 + gG_{cc}}, \tag{14}$$

$$\frac{\dot{w}_{c/nc}}{f_p} = G_{cp}. \tag{15}$$

The maximum reduction of vibration at the control position at the kth resonance frequency ω_k is therefore defined as

$$\rho_k = \frac{|\dot{w}_{c/c}/f_p(\omega_k)|}{|\dot{w}_{c/nc}/f_p(\omega_k)|} = \frac{1}{|1 + g_{\max}G_{cc}(\omega_k)|}, \tag{16}$$

where $g_{\max}$ is the maximum feedback control gain that guarantees stability which, approximately, can be taken as the reciprocal of the real part of the open loop sensor-actuator FRF, G_{cc}, at the fundamental natural frequency of the actuator $\omega_a = \sqrt{K_a/M_a}$:

$$g_{\max} \approx -\frac{1}{\mathrm{Re}\{G_{cc}(\omega_a)\}}. \tag{17}$$

The response at the resonance frequencies of the low order natural modes of the plate can also be approximated by the real parts of the open loop sensor-actuator FRF, G_{cc}, at the resonance frequencies, i.e., $G_{cc}(\omega_k) \approx \mathrm{Re}\{G_{cc}(\omega_k)\}$, so that the ratio ρ_k can be expressed as

$$\rho_k \approx \frac{1}{1 + \delta_{k0}}, \tag{18}$$

where $\delta_{k0} = \delta_k/\delta_0$ with $\delta_k = \mathrm{Re}\{G_{cc}(\omega_k)\}$ and $\delta_0 = -\mathrm{Re}\{G_{cc}(\omega_a)\}$, as shown in Fig. 4(b). Normally, the control performance ratio ρ_k is expressed in decibels with the following formula:

$$R_k = 20\log_{10}\left(\frac{1}{\rho_k}\right) \approx 20\log_{10}(1 + \delta_{k0}). \tag{19}$$

The stability and control performance effects are often analyzed separately. This simple expression contains both information on the stability and control performance of the feedback system. The stability-performance formulas in Eqs. (18) and (19) suggest that in order to maximize the control performance, the ratio $\delta_{k0} = \delta_k/\delta_0$, that is, the ratio between $\mathrm{Re}\{G_{cc}(\omega_k)\}$ and $-\mathrm{Re}\{G_{cc}(\omega_a)\}$, should be maximized.

The ratio $\delta_{k0} = \delta_k/\delta_0$ can be derived in a simplified form by making some assumptions about the driving point mobility function of the plate structure $Y_{cc}(\omega)$. In fact, assuming $\omega = \omega_a < \omega_1$, where ω_1 is the first natural frequency of the plate, the mobility function for $Y_{cc}(\omega)$ given in Eq. (5) can be approximated by

$$Y_{cc}(\omega_n) \approx \frac{j\omega_a}{K_p}, \tag{20}$$

where $1/K_p = \Sigma_{n=1}^{N}[\phi_n(x_c,y_c)]^2/M_p\omega_n^2$. Thus, using Eq. (12), the value of δ_0 is found to be

$$\delta_0 = -\mathrm{Re}\{G_{cc}(\omega_a)\} \approx \frac{\omega_a \psi}{2\zeta_a K_p - C_a\omega_a}. \tag{21}$$

Assuming now $\omega=\omega_k>\omega_a$, the mobility function for $Y_{cc}(\omega)$ in Eq. (5) can be approximated by

$$Y_{cc}(\omega_k) \approx \frac{1}{C_{p,k}}, \tag{22}$$

where $1/C_{p,k}=[\phi_k(x_c,y_c)]^2/M_p\omega_k\eta$. Thus, using Eq. (12), the value of δ_k is found to be

$$\delta_k = \mathrm{Re}\{G_{cc}(\omega_k)\} \approx \frac{\psi}{C_a + C_{p,k}}. \tag{23}$$

In conclusion, assuming $\omega=\omega_k>\omega_a$, where ω_k is the kth natural frequency of the plate, the maximum reduction of vibration at the control position given by Eq. (18) is found to be

$$\rho_k \approx \frac{\omega_a(C_{p,k}+C_a)}{\omega_a C_{p,k} + 2\zeta_a K_p}. \tag{24}$$

This simple expression indicates that the control performance of a velocity feedback control loop with a proof mass electrodynamic actuator for the well separated resonance frequencies of low order modes of the structure rises as the fundamental resonance frequency of the actuator decreases.

III. DOWNSCALING OF AN ELECTRODYNAMIC PROOF MASS ACTUATOR

Normally the downscaling study of a control system is carried out by assessing how the force generated by an actuator varies as the size of the actuator is scaled down. Although at first sight this looks as the right approach, it is also important to analyze how the stability and active control, i.e., active damping, effects vary with the downscaling of the actuator. In this way, it is possible to get an indication whether for decentralized control it would be convenient to use few, large scale, control units or many, small scale, control units over the surface of a panel. In the following sections, the downscaling laws for the principal components of the actuator are first revised. The downscaling laws for the actuator driving current, control force, and stroke are then considered. Finally, the stability-performance analysis presented in the previous section is used to assess how the maximum control performance varies with the downscaling of the actuator. As described by Madou,[20] the scaling laws are expressed with a $[L^n]$ notation, where n identifies the power of the linear dimension L. For those quantities that remain unchanged with scaling, a $[L^0]$ scaling law is assigned. For instance, the physical (mobility function and natural frequencies) and geometrical (dimensions) properties of the panel will have a scaling law $[L^0]$.

A. Scaling laws of the mechanical components of the actuator

According to the schematic shown in Fig. 1(b) and the analytical formulation for the response of the system presented in Sec. II, the principal mechanical components of the actuator are the proof mass, the suspension system, and, although it does not correspond to a self-contained mechanical component, the viscous damper which describes the damping effect produced by the squeeze film of lubricant between the guiding stinger and the central hole in the proof mass [see Fig. 1(a)]. The scaling laws for the mass, stiffness, and damping effects of these three components can be derived by inspection of the formulas for these quantities.

Despite the cross section of the magnet proof mass is rather involved, it can be readily shown that its scaling law is

$$M_a \propto [L^3].$$

In order to minimize the deformation stress effect in the mounting spring,[21] a spring with ring shape has been chosen for the suspension of the mass in the prototype system studied in this paper. According to Young and Budynas,[22] the stiffness of a ring to a diametric load is given by

$$K_a = \frac{EI}{R^3}\left(\frac{4\pi}{k_1\pi^2 - 8k_2^2}\right), \tag{25}$$

where E is Young's modulus of the material of the spring, R is the radius of the ring, I is the area moment of the cross section of the ring (for rectangular section of dimensions $b \times h$, it is $I=bh^3/12$), and k_1, k_2 are the dimensionless constants.[22] As a result, the scaling law for the suspension system is given by

$$K_a \propto [L^1].$$

Finally, the coefficient for the damping effect produced by the squeeze film of lubricant between the guiding stinger and the central hole in the proof mass results directly proportional to the linear dimension;[23] thus,

$$C_a \propto [L^1].$$

In conclusion, as graphically summarized in Fig. 5(a), as the sizes of the actuator are scaled down the stiffness and damping coefficient falls down with power 1 of L while the mass effectively falls down with power 3 of L.

B. Electrodynamic actuation force scaling laws

The scaling laws of the actuation force produced by a coil-magnet actuator have been presented by Trimmer[24] who has considered three cases: (a) constant current density, J_a, in the coil; (b) constant heat flow, ΔQ, per unit surface area of the windings in the coil, and (c) constant temperature difference, ΔT, between the windings of the coil and the surrounding environment. For these three cases, the scaling of current density, J_a, in the windings of the coil with reference to dimension is given by the following:

(a) constant J_a $J_a \propto [L^0]$,
(b) constant ΔQ $J_a \propto [L^{-0.5}]$, and
(c) constant ΔT $J_a \propto [L^{-1}]$.

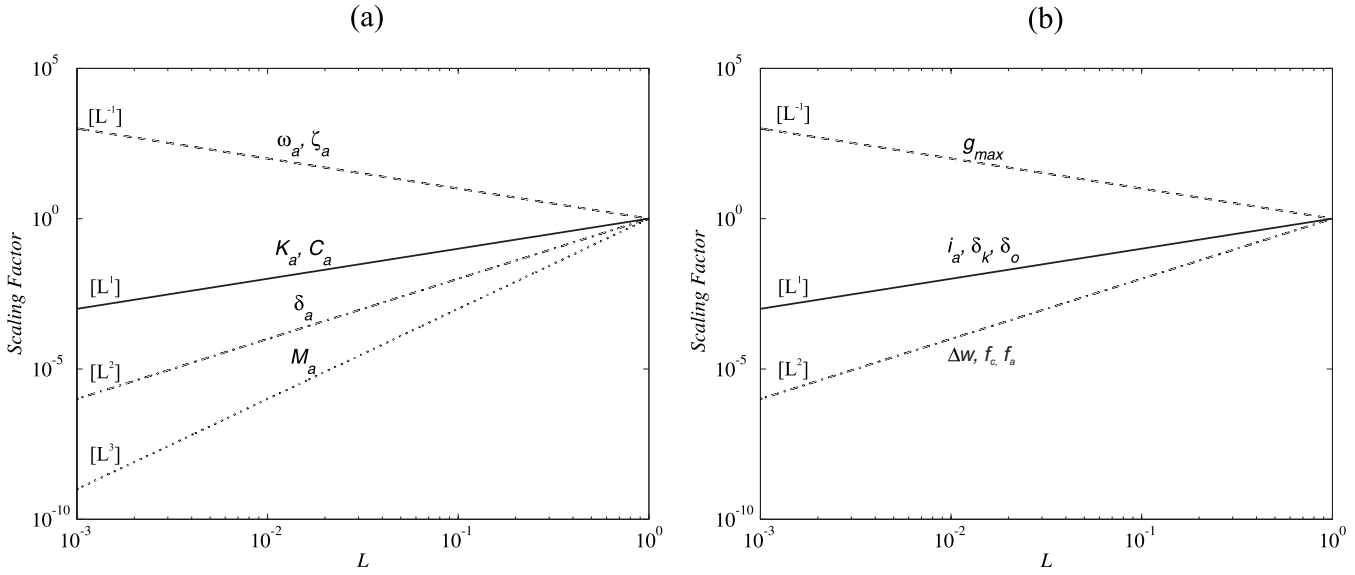

FIG. 5. Scaling laws. (a) Mass M_a, damping factor C_a, stiffness K_a, fundamental natural frequency ω_a, static displacement δ_a, and damping ratio ζ_a. (b) Driving current i_a, electrodynamic actuation force f_a, force transmitted to the base of the actuator f_c, stroke of the suspended mass Δw, δ_0, and δ_k functions, and maximum control gain $g_{\max}$.

In practice, the most relevant case, which is considered in the remaining part of the paper, is that for constant temperature difference since, normally, it is high temperature that causes coil windings to fail. As shown by the block diagram in Fig. 3, the feedback loop considered in this study drives the actuator with a current signal. The current in the winding of the actuator coil is given by $i_a=J_aA$, where A is the cross sectional area of the winding. Thus, the scaling law of the current that can be fed to the coil of the actuator with reference to dimension is given by

$$|i_a| \propto [L^1].$$

Assuming the proof mass is made of a permanent magnet cylindrical core with an outer ferromagnetic ring [see Fig. 1(a)] that, because of its cross sectional shape, generates a constant magnetic field B across the windings of the coil, the actuation force f_a is given by Eq. (8) with the voice coil coefficient given by $\psi=Bl$, where l is the total length of the windings. Thus,

$$f_a = -Bli_a. \tag{26}$$

As a result, considering constant ΔT between windings and environment and assuming that B scales with $[L^0]$, the scaling law of the actuation force is given by

$$|f_a| \propto [L^2].$$

In summary, as shown in Fig. 5(b), as the size of the actuator is scaled down the current that can be fed to drive a coil-magnet motor i_a falls down with power 1 of L and the force generated by a coil-magnet linear motor f_a falls down with power 2 of L.

C. Scaling laws of the static and dynamic characteristics of the proof mass actuator

The principal static and dynamic characteristics of the proof mass actuator are given by its fundamental natural frequency, static displacement, and damping ratio, which are given by the following expressions:

$$\omega_a = \sqrt{\frac{K_a}{M_a}}, \tag{27a}$$

$$\delta_a = \frac{M_a g}{K_a}, \tag{27b}$$

$$\zeta_a = \frac{C_a}{2\sqrt{K_a M_a}}. \tag{27c}$$

Thus, the scaling laws for these three functions are given by

scaling of ω_a: $\omega_a \propto [L^{-1}]$,

scaling of δ_a: $\delta_a \propto [L^2]$,

scaling of ζ_a: $\zeta_a \propto [L^{-1}]$.

As shown in Fig. 5(a), these three expressions indicate that as the size of the actuator is scaled down, the fundamental natural frequency and the damping ratio tend to rise with power 1 of L, while the static displacement falls down with power 2 of L. The first effect is undesirable since, as we have seen in Sec. II, it is of critical importance to design the actuator with the smallest possible fundamental natural frequency. In contrast, the fact that the static displacement falls down with the square of downscaling is a positive effect. Finally, the increase of the damping ratio in proportion to the downscaling should also be regarded as a positive effect since, according to the discussion presented in Sec. II, the closer is the damping to the critical damping factor, the

smaller is likely to be the amplitude at the fundamental resonance of the actuator and thus the higher should be the maximum control gain for a stable feedback control loop.

The last two fundamental characteristics of the proof mass actuator to be assessed are the stroke of the suspended mass $\Delta w = w_m - w_c$ and the force it can transmit to the base f_c. To ensure a correct operation of the actuator, the stroke of the suspended mass should be kept within the linear deflection range of the axial springs; thus, it should fall down with power 1 of L as the size of the actuator is scaled down, i.e., $|\Delta w| \propto [L^1]$. Thus, recalling the direct relation between the control force and the stroke of the suspended mass given in Eq. (11), also the control force should fall down with power 1 of L as the size of the actuator is scaled down, i.e., $|f_c| \propto [L^1]$. However, Eqs. (9) and (10) indicate that the stroke of the suspended mass and the force transmitted to the base depend on the current driving the actuator i_a, which was found to fall down with power 1 of L as the actuator is scaled down. Thus, the downscaling of the stroke of the suspended mass and control force should also be analyzed with respect to the downscaling of the current driving the actuator. As shown in Fig. 2(b), the maximum stroke of the actuator occurs at its fundamental resonance frequency, i.e., for $\omega = \omega_a$, in which case Eq. (10) reduces to

$$\Delta w = \frac{(\omega_a/K_a + jY_{cc})}{C_a\omega_a Y_{cc} - j(2\zeta_a\omega_a + K_a Y_{cc})}\psi i_a, \tag{28}$$

so that, considering constant ΔT between windings and environment, the scaling law for the stroke is given by

$$\text{Scaling of } |\Delta w|\text{: } |\Delta w| \propto [L^2].$$

The actuator is designed to implement the velocity feedback loop above its fundamental resonance frequency, i.e., for $\omega > \omega_a$, in which case Eq. (9) reduces to

$$f_c = \frac{\psi}{1 + Z_a Y_{cc}} i_a, \tag{29}$$

Thus, considering constant ΔT between windings and environment, the scaling law for the control force is given by

$$\text{Scaling of } |f_c|\text{: } |f_c| \propto [L^2].$$

Hence, it is the current that can be fed to the actuator rather than the linear deflection range of the axial springs that determines the downscaling laws for the stroke of the suspended mass and the force transmitted to the base of the actuator. As shown in Fig. 5(b), as the size of the actuator scales down, the stroke of the proof mass falls down with power 2 of L. Also, above the fundamental resonance frequency of the proof mass actuator, as the size of the actuator scales down, the force transmitted to the base of the actuator $|f_c|$ falls down with power 2 of L.

D. Scaling laws for the stability and performance of the velocity feedback loop

As discussed in Sec. II C, assuming the downscaling is limited to values such that the fundamental resonance frequency of the proof mass actuator is below the first resonance of the panel, the downscaling effect on the maximum control performance of the velocity feedback loop using the proof mass actuator can be assessed with Eq. (19): $R_k = 20\log_{10}(1+\delta_{k0})$. The scaling of the ratio $\delta_{k0} = \delta_k/\delta_0$ can be readily derived by substituting in Eqs. (21) and (23) the scaling laws for the mechanical components and the dynamic characteristics of the actuator, which gives

$$\text{Scaling of } \delta_0 = -\text{Re}\{G_{cc}(\omega_a)\} \quad \delta_0 \propto [L^1].$$

$$\text{Scaling of } \delta_k = \text{Re}\{G_{cc}(\omega_k)\} \quad \delta_k \propto [L^1].$$

Thus, as shown in Fig. 5(b), both terms fall down with power 1 of L as the size of the actuator is scaled down. As a result, the ratio $\delta_{k0} = \delta_k/\delta_0$, and consequently the control performance ratio R_k, should not change with the downscaling of the actuator. However, the control performance ratio derived with Eq. (19) refers to the maximum feedback control gain that guarantees a stable feedback control loop, which according to Eq. (17) is given by $g_{\max} = 1/\delta_0$. Thus, as shown in Fig. 5(b), it implies that the maximum control gain rises with power of 1 of L as the actuator size is scaled down:

$$\text{Scaling of } g_{\max} = 1/\delta_0 \quad g_{\max} \propto [L^1].$$

As a result, the current i_a feedback to the actuator should also rise with power 1 of L as the actuator size is scaled down. However, as highlighted in Sec. III B, the maximum current i_a that can be fed to a coil-magnet actuator falls down with power 1 of L as the actuator size is scaled down. Thus, the effective scaling law of the control performance should be assessed assuming $g_{\max} \propto [L^1]$, and thus $\delta_0 \propto [L^{-1}]$, in which case the scaling law for the control performance index is given by

$$\text{Scaling of } R_k = 20\log_{10}(1+\delta_{k0}) \quad R_k \propto [L^2].$$

Thus, as shown in Fig. 6, the control performance of a velocity feedback loop using a proof mass electrodynamic actuator falls down with power 2 of L as the size of the actuator is scaled down. It should be emphasized that this loss of control performance is purely due to the limitation of current that can be fed to the coil-magnet actuator as the size is

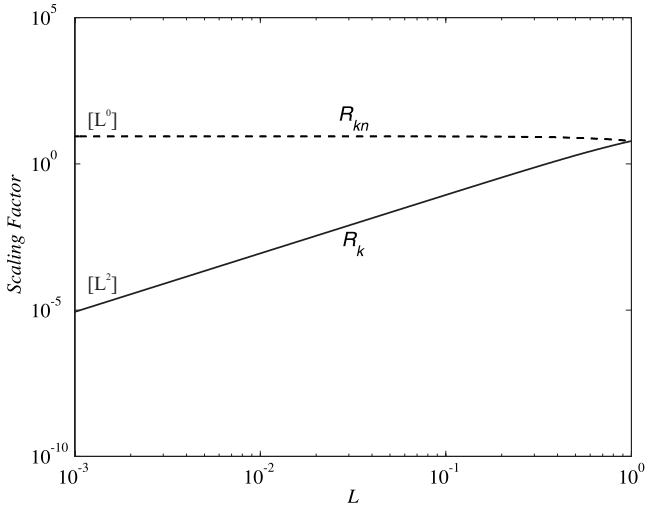

FIG. 6. Scaling laws for the control performance ratio considering one control units R_k and n decentralized control units R_{kn}.

scaled down. In other words, as the control actuator is scaled down, the feedback control gain that can be implemented in practice is much lower than the maximum value that would guarantee stability.

The number of control units that can be fitted per unit surface of the plate structure grows with power 2 or L as the size of the units is scaled down, i.e., $n \propto [L^{-2}]$; thus, the overall control performance that would be produced by n feedback control loops R_{kn} should remain constant. However, as highlighted above, the feedback control loops would be used increasing gain margins which guarantees more robust feedback loops. Bauman and Elliott[25] have highlighted that the control performance of multiple feedback loops tends to degrade as the number of control units rises because of instability issues generated by cross-talking effects between neighbor actuators. Thus, if small scale control units that operate with large gain margins were to be used, this problem could be less pronounced and thus better control performance can be obtained with dense arrays of small scale control units rather than with fewer large scale control units.

It is important to emphasize that these speculations are based on the assumption that the fundamental resonance frequency of the actuator is lower than the first resonance of the panel which, as discussed in Sec. III C, rises with power 2 of L. Thus, it is likely that there is an optimal trade-off between the number, size, mechanical properties, and gain margin of the control units that would produce the best control performance effect.

IV. DESIGN AND TESTING OF A PROTOTYPE SMALL SCALE PROOF MASS ACTUATOR FOR VELOCITY FEEDBACK CONTROL

This section introduces the design and testing of a prototype small scale electrodynamic proof mass actuator that has been used to implement a velocity feedback control loop on a clamped rectangular panel whose properties are summarized in Table I. The panel is excited by a point force produced by a shaker located underneath the panel at $x_p = 341$ mm, $y_p = 246$ mm. The actuator is positioned on the top of the panel at $x_c = 109$ mm, $y_c = 75$ mm. In order to implement a velocity feedback control loop, a small accelerometer sensor is located underneath the panel at the center of the actuator footprint. The velocity feedback loop is implemented with an analog controller which is composed by an integrator to get the error velocity signal, a dc decoupling high pass filter with corner frequency at about 10 Hz, and a current amplifier.

The stability analysis of the feedback control loop has been carried out following the methodology presented in Sec. II B. The control performance has been assessed by plotting the spectrum of the response at the control position per unit primary force excitation in a frequency range between 0 and 1 kHz.

A. Prototype small scale proof mass actuator

Following the guidelines of the scaling study presented in Sec. III, the miniaturization of the prototype actuator has been carried out up to a limit such that the fundamental natural frequency of the suspended mass remains below the first resonance frequency of the plate under control. The first resonance of the rectangular panel considered in this study is at about 73 Hz. Thus, it has been decided to design the proof mass and suspension spring system such that the fundamental resonance of the actuator is around 20 Hz. A trial and error approach has been used to identify the dimensions of the components of the actuator. In addition to the physical restraints derived from the scaling study, the design of the prototype actuator has also been constrained by fabrication limitations due to the manufacturing machine tools available in the laboratory.

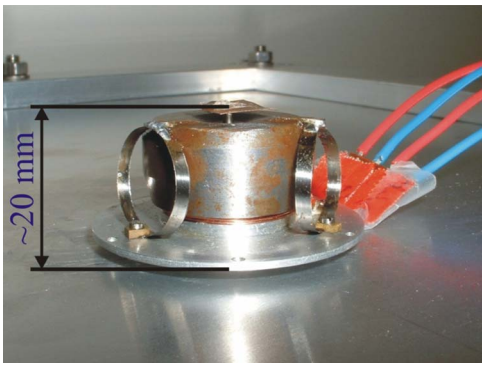

FIG. 7. (Color online) Photo of the small scale electrodynamic proof mass actuator.

The small scale prototype electrodynamic proof mass actuator designed and built for this study is shown in Fig. 7. The physical and geometrical properties of the actuator are summarized in Table II. As schematically shown in Fig. 1(a), this actuator is composed of a base disk with a cylindrical former on which the coil is wound. The proof mass is formed by a magnetic core cylinder and an outer ferromagnetic ring. The proof mass is mounted on three springs and a vertical bushing, which forces the magnet to oscillate in the axial direction.

As shown in Fig. 7, the three springs are made of small circular rings which guarantee a relatively larger stiffness in the transverse direction than in the axial direction. In this way, the fundamental axial natural frequency of the proof mass actuator can be kept rather low with a good transverse guiding which prevents nonlinear effects due to the stick slip friction on the axial bushing. As shown in Fig. 1(a), the cross section of the magnet is shaped in such a way as to have a magnetic circuit that generates a field oriented in the direction orthogonal to the coil winding. In this way, a current flow through the coil produces the reactive axial force between the coil and the magnet which is given by Eq. (8). The details of the design of the circular springs and coil-magnet transducers are presented by Paulitsch.[21]

B. Open loop stability analysis

The Bode plot in Fig. 8 shows the measured open loop sensor-actuator FRF. The plot shows that there is nearly no peak of the fundamental resonance of the actuator at about 20 Hz. As discussed in Sec. II B, this is due to the fact that the fundamental resonance of the actuator is well below the

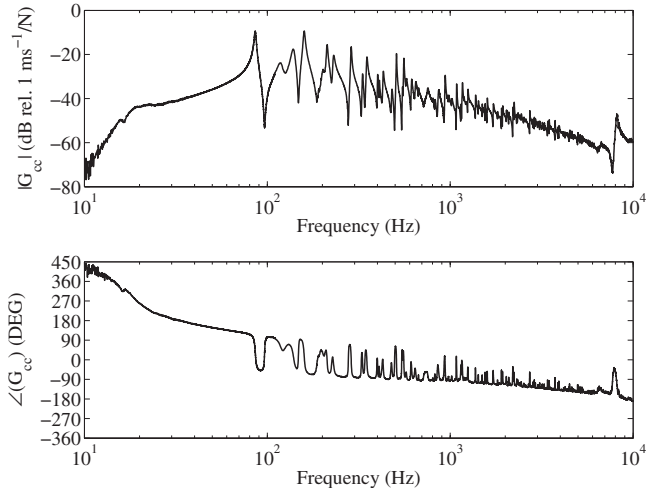

FIG. 8. Measured Bode plot of the open loop frequency response function between the error sensor signal and the input signal to the analog controller of the feedback loop.

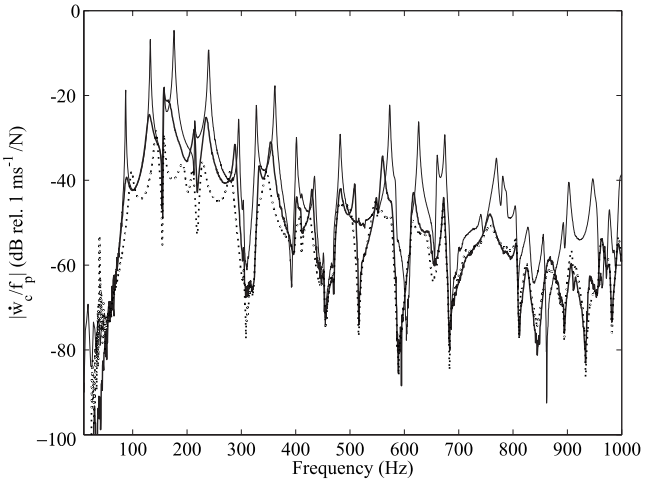

FIG. 10. Measured velocity at the error sensor position per unit primary force without actuator (faint line), with actuator and no control (thick line), with actuator when a gain margin of 6 dB (dotted line) is implemented.

first resonance of the panel and to the fact that there is a rather high internal mechanical damping effect in the actuator. Also, a high pass filter used to implement dc decoupling has been used in the feedback loop, which contributes to lower the amplitude of the actuator fundamental resonance. Between 60 Hz and 1 kHz, the FRF is characterized by a sequence of lightly damped plate resonances. At higher frequencies, there is a constant amplitude roll-off with frequency of the FRF, which is due to the inertial effect of the base disk and coil components of the actuator. At about 6 kHz, there is a deep trough followed by a sharp resonance peak. A finite element analysis of the base disk and cylindrical former has shown a resonance frequency in a similar frequency range. At higher frequencies, two other resonances are visible, which are due to the flexible modes of the circular springs.

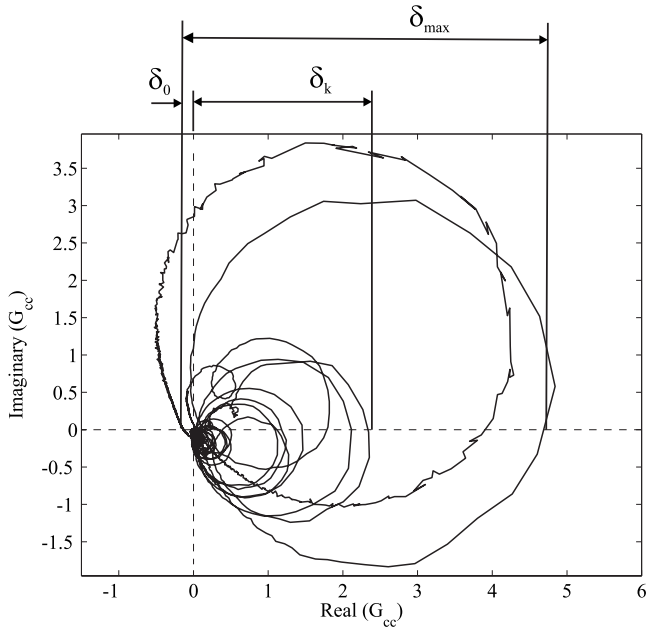

FIG. 9. Measured Nyquist plot of the open loop frequency response function between the error sensor signal and the input signal to the analog controller of the feedback loop.

The Nyquist plot in Fig. 9 shows the measured open loop sensor-actuator FRF. The plot shows a small semicircle on the left hand side which is due to the heavily damped fundamental resonance of the actuator and the high pass filter for the dc decoupling. There are then a number of circles on the right hand side which are due to the plate resonances of the low order modes of the plate. The phase lag effect generated by the inductive effect of the coil gradually drifts the loci toward the imaginary axis in the bottom right quadrant so that the large circle for the base disk and cylindrical former resonance is oriented along the imaginary negative axis. At higher frequencies, the locus enters the left hand side quadrants but, because of the roll-off effect produced by the inertia of the base disk and coil components of the actuator, the amplitude is relatively small compared to the low frequency part of the locus located on the positive real quadrants. In conclusion, the control system is bound to be conditionally stable with a maximum control gain that guarantees stability $g_{\max}=4.5$.

As discussed in Sec. II C, the Nyquist plot in Fig. 9 can also be used to estimate the maximum reduction of vibration at the control position that can be achieved at a certain resonance frequency of the panel. For the kth resonance frequency, the maximum reduction of vibration in decibels is given by $R_k=20\log_{10}|1+\delta_k/\delta_0|$, so that for the largest resonance circle at about 180 Hz the maximum reduction is predicted to be about 20 dB.

C. Closed loop control performance analysis

The plot in Fig. 10 shows the spectrum of velocity measured by the error sensor per unit excitation force. The faint line in the plot shows that the response at the error sensor when the actuator is not mounted on the panel is characterized by well separated sharp resonance peaks in nearly the whole frequency range considered. When the actuator is mounted on the plate, the resonance peaks are slightly

moved down in frequency and, more importantly, are rounded off by the passive damping effect produced by the actuator (thick line). At frequencies above the fundamental resonance frequency of the actuator, the actuator proof mass acts as an inertial reference so that, if the mechanical and electromechanical damping (due to the back emf in the coil) in the actuator are subcritical, additional passive damping is injected to the plate.[26] The constant roll-off is due to the inertial effect of the base disk and coil components of the actuator. When the feedback loop is closed with a gain margin of about 6 dB that guarantees stability and low control spillover effect around the fundamental resonance frequency of the proof mass actuator, as shown by the dotted line, between 80 and 250 Hz, the vibration at the error sensor goes down by 5–10 dB. However, at very low frequency, there is some control spillover effect which, as discussed in Sec. II A, is due to the low frequency smooth −180° phase transition of the actuation force per unit driving current signal.

V. CONCLUDING REMARKS

This paper has introduced the stability and performance study of a small scale prototype proof mass actuator for the implementation of a direct velocity feedback loop on a thin panel structure. A stability-performance formula that can be used to assess simultaneously the stability and control performance of the feedback control loop with the proof mass actuator has been derived from a mobility/impedance formulation. The principal downscaling and design issues of the proof mass actuator have then been analyzed in view of the stability requirements and control performance properties of the feedback loop. The principal outcome of this study has highlighted that the downscaling of a proof mass actuator using an electrodynamic linear motor produces both positive and negative effects. Among the positive effects are the reduction of the static displacement δ_a and stroke Δw and the increment of the damping ratio ζ_a, which scale, respectively, with $[L^2]$, $[L^2]$, and $[L^{-1}]$. Alternatively, among the negative effects are the rise of the fundamental natural frequency ω_a and decrement of the current driving the actuator i_a and the control f_a and transmitted f_c forces by the actuator, which scale, respectively, with $[L^{-1}]$, $[L^1]$ and $[L^2]$, $[L^2]$. Assuming the downscaling is limited to values such that the fundamental resonance frequency of the proof mass actuator is below the first resonance of the rectangular panel, the reduction of vibration for the maximum control gain that guarantees a stable feedback control loop remains constant. However, since the maximum current that can be fed to the actuator scales with $[L^1]$, also the control gain must be scaled with $[L^1]$ so that the control performance also falls down with power 2 of L as the size of the actuator is scaled down. This limitation is, however, mitigated by the fact that the number of control units that can be fitted per unit surface of the panel increases with power 2 of L as the actuators are scaled down so that the overall control performance with multiple decentralized control units would remain constant.

In the second part of the paper, the design of a small scale prototype actuator with a fundamental natural frequency $\omega_a = 20$ Hz well below the first resonance of the panel at about 73 Hz has been introduced. The stability and control performance of one direct velocity feedback control unit with such an actuator mounted on a thin rectangular panel which is clamped on a rigid frame have been assessed experimentally. When the feedback control loop is closed with a gain margin of 6 dB, so that there is little control spillover effect around the fundamental resonance of the actuator, reductions of vibration between 5 and 10 dB in the frequency band between 80 and 250 Hz have been measured at the control position.

ACKNOWLEDGMENTS

The work done by C.G.D. and C.P. for this project was supported by the "Early Stage Training site Marie Curie" program for the "European Doctorate in Sound and Vibration Studies" (EDSVS), which is funded by the European Commission. The prototype actuator studied in this paper was built in collaboration with Rene' Boonen at Katholieke Universiteit Leuven.

[1] D. J. Thompson and J. Dixon, "Vehicle noise," in *Advanced Applications in Acoustics, Noise and Vibration*, edited by F. J. Fahy and J. G. Walker (E & FN Spon, London, 2004), Chap. 6, pp. 236–291.
[2] J. S. Mixson and J. S. Wilby, "Interior noise," in *Aeroacoustics of Flight Vehicles, Theory and Practice*, edited by H. H. Hubbard (NASA Langley Research Center Hampton, Virginia, 1995), Chap. 16, pp. 271–335.
[3] P. Gardonio, "Review of active techniques for aerospace vibro-acoustic control," J. Aircr. **39**, 206–214 (2002).
[4] F. J. Fahy, "Fundamentals of noise and vibration control," in *Fundamentals of Noise and Vibration*, edited by F. J. Fahy and J. G. Walker (E & FN Spon, London, 1998), Chap. 5, pp. 255–309.
[5] M. J. Brennan and N. S. Ferguson, "Vibration Control," in *Advanced Applications in Acoustics, Noise and Vibration*, edited by F. J. Fahy and J. G. Walker (E & FN Spon, London, 2004), Chap. 12, pp. 530–580.
[6] S. J. Elliott, P. Gardonio, T. C. Sors, and M. J. Brennan, "Active vibroacoustic control with multiple local feedback loops," J. Acoust. Soc. Am. **111**, 908–915 (2002).
[7] F. J. Fahy and P. Gardonio, *Sound and Structural Vibration: Radiation, Transmission and Response*, 2nd ed. (Academic, London, 2007).
[8] E. Bianchi, P. Gardonio, and S. J. Elliott, "Smart panel with multiple decentralized units for the control of sound transmission. Part III: Control system implementation," J. Sound Vib. **274**, 215–232 (2004).
[9] C. R. Fuller, S. J. Elliott, and P. A. Nelson, *Active Control of Vibration* (Academic, New York, 1996).
[10] P. Gardonio and S. J. Elliott, "Smart panels for active structural acoustic control," Smart Mater. Struct. **13**, 1314–1336 (2004).
[11] R. L. Clark, W. R. Saunders, and G. P. Gibbs, *Adaptive Structures*, 1st ed. (Wiley, New York, 1998).
[12] A. Preumont, *Vibration Control of Active Structures*, 2nd ed. (Kluwer, London, 2002).
[13] M. J. Balas, "Direct velocity feedback control of large space structures," J. Guid. Control **2**, 252–253 (1979).
[14] V. Jayachandran and J. Q. Sun, "Unconditional stability domains of structural control systems using dual actuator-sensor pairs," J. Sound Vib. **208**, 159–166 (1997).
[15] S. J. Elliott, M. Serrand, and P. Gardonio, "Feedback stability limits for active isolation systems with reactive and inertial actuators," J. Vibr. Acoust. **123**, 250–261 (2001).
[16] P. Gardonio and M. J. Brennan, "Mobility and impedance methods in structural dynamics," in *Advanced Applications in Acoustics, Noise and Vibration*, edited by F. J. Fahy and J. Walker (E & FN Spon, London, 2004), Chap. 9, pp. 387–388.
[17] L. Meirovitch, *Dynamics and Control of Structures* (Wiley, New York, 1990).
[18] O. N. Baumann and S. J. Elliott, "Destabilization of velocity feedback controllers with stroke limited inertial actuators," J. Acoust. Soc. Am. **121**, 211–217 (2007).
[19] P. Gardonio and S. J. Elliott, "Modal response of a beam with a sensor-actuator pair for the implementation of velocity feedback control," J.

Sound Vib. **284**, 1–22 (2005).
[20]M. J. Madou, *Fundamentals of Microfabrication: The science of Miniaturization*, 1st ed. (CRC, Boca Raton, FL, 1997).
[21]C. Paulitsch, "Vibration control with electrodynamic actuators," Ph.D. thesis, ISVR, University of Southampton, 2005.
[22]W. C. Young and R. G. Budynas, *Roark's Formulas for Stress and Strain*, 6th ed. (McGraw-Hill, New York, 1989).
[23]J. Peirs, "Design of micromechatronic systems: scale laws, technologies, and medical applications," Ph.D. thesis, Katholieke Universiteit Leuven, 2001.
[24]W. S. N. Trimmer, "Microrobots and micromechanical systems," Sens. Actuators **19**, 267–287 (1989).
[25]O. N. Baumann and S. J. Elliott, "The stability of decentralized multichannel velocity feedback controllers using inertial actuators," J. Acoust. Soc. Am. **121**, 188–196 (2007).
[26]C. Paulitsch, P. Gardonio, and S. J. Elliott, "Active vibration damping using an inertial, electrodynamic actuator (DETC2005-84632)," ASME J. Vibr. Acoust. **129**, 39–47 (2007).